remote sensing

MDPI

Article

Improving Accuracy Estimation of Forest Aboveground Biomass Based on Incorporation of ALOS-2 PALSAR-2 and Sentinel-2A Imagery and Machine Learning: A Case Study of the Hyrcanian Forest Area (Iran)

Sasan Vafaei [1], Javad Soosani [1,*], Kamran Adeli [1], Hadi Fadaei [2], Hamed Naghavi [1], Tien Dat Pham [3] and Dieu Tien Bui [4,*]

1 Faculty of Agriculture and Natural Resources, Lorestan University, Khorramabad, Lorestan 68151-44316, Iran; sasan.vafaei@gmail.com (S.V.); adeli.k@lu.ac.ir (K.A.); Naghavi.Ha@lu.ac.ir (H.N.)
2 Department of Social Informatics, Graduate School of Informatics, Kyoto University, Kyoto 606-8501, Japan; fadaei@bre.soc.i.kyoto-u.ac.jp
3 Center for Agricultural Research and Ecological Studies (CARES), Vietnam National University of Agriculture (VNUA), Trau Quy, Gia Lam, Hanoi 10000, Vietnam; dat6784@gmail.com
4 Geographic Information System Group, Department of Business and IT, University College of Southeast Norway, N-3800 Gullbringvegen 36, Bø i Telemark, Norway
* Correspondence: Soosani.j@lu.ac.ir (J.S.); Dieu.T.Bui@usn.no (D.T.B.)

Received: 28 October 2017; Accepted: 23 January 2018; Published: 25 January 2018

Abstract: The main objective of this research is to investigate the potential combination of Sentinel-2A and ALOS-2 PALSAR-2 (Advanced Land Observing Satellite -2 Phased Array type L-band Synthetic Aperture Radar-2) imagery for improving the accuracy of the Aboveground Biomass (AGB) measurement. According to the current literature, this kind of investigation has rarely been conducted. The Hyrcanian forest area (Iran) is selected as the case study. For this purpose, a total of 149 sample plots for the study area were documented through fieldwork. Using the imagery, three datasets were generated including the Sentinel-2A dataset, the ALOS-2 PALSAR-2 dataset, and the combination of the Sentinel-2A dataset and the ALOS-2 PALSAR-2 dataset (Sentinel-ALOS). Because the accuracy of the AGB estimation is dependent on the method used, in this research, four machine learning techniques were selected and compared, namely Random Forests (RF), Support Vector Regression (SVR), Multi-Layer Perceptron Neural Networks (MPL Neural Nets), and Gaussian Processes (GP). The performance of these AGB models was assessed using the coefficient of determination (R^2), the root-mean-square error (RMSE), and the mean absolute error (MAE). The results showed that the AGB models derived from the combination of the Sentinel-2A and the ALOS-2 PALSAR-2 data had the highest accuracy, followed by models using the Sentinel-2A dataset and the ALOS-2 PALSAR-2 dataset. Among the four machine learning models, the SVR model (R^2 = 0.73, RMSE = 38.68, and MAE = 32.28) had the highest prediction accuracy, followed by the GP model (R^2 = 0.69, RMSE = 40.11, and MAE = 33.69), the RF model (R^2 = 0.62, RMSE = 43.13, and MAE = 35.83), and the MPL Neural Nets model (R^2 = 0.44, RMSE = 64.33, and MAE = 53.74). Overall, the Sentinel-2A imagery provides a reasonable result while the ALOS-2 PALSAR-2 imagery provides a poor result of the forest AGB estimation. The combination of the Sentinel-2A imagery and the ALOS-2 PALSAR-2 imagery improved the estimation accuracy of AGB compared to that of the Sentinel-2A imagery only.

Keywords: aboveground biomass; ALOS-2 PALSAR-2; Sentinel-2A; random forest; support vector regression; gaussian processes; neural networks; Hyrcanian forest; Iran

1. Introduction

Forests play an important role in the global carbon cycle for reducing carbon dioxide concentrations, which further mitigates the impact of global warming and climate change [1–3]. Unfortunately, forests have been destroyed worldwide with a loss of around 2.3 million km^2 from 2000 to 2012, which resulted in carbon stocks losses [4]. As such, accurate measurement of forest carbon stocks and aboveground biomass (AGB) is considered key for understanding the global carbon cycle, for evaluating emissions from deforestation, and for regional, sustainable land-use planning [5,6].

Numerous studies have been conducted to estimate forest AGB. These studies could be grouped into destructive methods and non-destructive methods. Although destructive approaches such as field measurements are considered to be the most accurate method for estimating AGB, they are time-consuming and costly. In addition, they may not be feasible for a large-scale analysis [7], particularly in regions of dense and mixed forests (i.e., in tropical and subtropical mountainous areas). Thus, the development of accurate and low-cost models to estimate the forest biomass is still greatly needed to support global climate change mitigation programs such as the United Nations' Reducing Emissions from Deforestation and Forest Degradation in Developing Countries (REDD+) scheme [8,9].

For forest AGB modeling, remotely sensed data has been widely used. Accordingly, the forest AGB is estimated through regression models, which are constructed based on direct relationships between AGB and spectral reflectance values derived from remotely sensed data. However, acceptable accuracy for estimating the forest AGB is still an obstacle in many areas [6,10]. In terms of optical data, the main drawback of the AGB estimation is due to the characteristics of forests such as close canopy, high diversity, and other complex structures [11,12]. Consequently, the optical data may become saturated and may be less sensitive in high biomass regions, resulting in challenges for accurately estimating AGB [13,14]. Compared to the optical data, SAR (Synthetic Aperture Radar) data has proven to be more effective in monitoring forest disturbance dynamics because SAR sensors can penetrate clouds that are common in the tropical area [15,16].

Among SAR image data, L-band is the most widely used for estimating forest AGB due to its sensitivity to woody components [17,18]. However, the L-band is only efficient for a certain range of AGB, and outside that range, the signal is saturated [19]. To overcome this limitation, integrating multi-source data such as optical images and SAR has been proposed to enhance the accuracy of the forest AGB estimation [20,21]. These combinations can be carried out in two ways: (i) data fusion of both SAR and optical images into a new dataset (i.e., principal component analysis (PCA) or wavelet transforms) [22]; and (ii) incorporation of all images [20]. However, there is still a debate on the accuracy the AGB estimation using SAR combined with optical data. Cutler et al. [23] pointed out that the combination of Multispectral Landsat TM (Thematic Mapper) and JERS (Japanese Earth Resources Satellite) SAR data may produce more precise results. Inversely, Hame et al. [24] concluded that the combination of optical ALOS AVNIR (Advanced Land Observing Satellite Advanced Visible and Near Infrared Radiometer) data and ALOS PALSAR (Phased Array type L-band Synthetic Aperture Radar) did not improve the accuracy of the biomass estimation. Therefore, further investigations on the combination of the optical data and SAR data for the AGB estimation should be carried out to gather more evidence and reach reasonable conclusions.

The recent launches of the new generation ALOS-2 PALSAR-2 (24 May 2014) by the Japan Aerospace Exploration Agency (JAXA) and the Sentinel-2A satellite (23 June 2015) by the European Space Agency (ESA) have provided new opportunities for forest AGB studies. The ALOS-2 PALSAR-2 offers radar imagery with dual-polarizations HH+HV or full-polarizations HH+HV+VH+VV in L-band [25], whereas the Sentinel-2A provides 12 multispectral bands [26]. The radar imagery has encouraged new approaches for developing more accurate models for estimating AGB. Investigation of the ALOS-2 PALSAR-2 for the forest AGB estimation is still rare. However, a recent study on the use of the Sentinel-2A MSI (Multi Spectral Instrument) data for the AGB estimation shows high accuracy [27]. In addition, the Sentinel-2A MSI sensor yields better results than that of Landsat 8 OLI for measuring forest canopy cover and leaf area index (LAI) [28] and for the AGB estimation of grasses [27].

Thus, compared to Landsat series, the Sentinel-2 sensor provides more spectral bands including visible and near infrared (VNIR) bands and better spatial resolutions 10–20 m than those of the Landsat data. More recently, combining Sentinel-2A imagery and the Sentinel-1 (SAR) imagery for AGB estimation was carried out, and it was concluded that this combination could be used for estimating AGB [29]. Nevertheless, study of the integration of the ALOS-2 PALSAR-2 and the Sentinel-2A data for estimating forest AGB has not been conducted regularly.

We address this gap in the literature in this paper by investigating the integration of the ALOS-2 PALSAR-2 and the Sentinel-2A MSI data for estimating the forest AGB with a case study of the Hyrcanian forest of Iran. The combination of the ALOS-2 PALSAR-2 and the Sentinel-2 MSI data was used because the ALOS-2 PALSAR-2 sensor has long wavelengths that penetrate into forest canopies, whereas the Sentinel-2A sensor has multispectral bands representing the canopy cover reflection of different species. Regardless, no method is best for estimating AGB in all areas. Therefore, in this work, four state-of-the-art machine learning methods including Random Forest (RF), Support Vector Regression (SVR), Multi-Layer Perceptron Neural Network (MLP Neural Net), and Gaussian Processes (GP) were used for building AGB models. These machine learning methods were selected because they have proven to be effective for forest AGB estimation in various investigations [30–32]. It is noted that the four machine learning algorithms are available at Weka open source software [33]. In addition, a python application developed by the authors was used to transfer the predicted AGB results to the GIS (Geographic Information System) environment.

2. Study Area and Data Used

2.1. Description of the Study Area

We conducted this study in the Hyrcanian forests, which belong to the Gilan province located in northern Iran (Figure 1). This area has a subtropical climate where the monthly average temperature is 14 °C and the annual precipitation is 1100 mm. The topography of Gilan is characterized by high mountainous terrains in the west and the south areas, while the terrain is flat in the north. According to our survey, the forest in Gilan covers an area of 564,712 ha with closed canopy and is characterized by a broadleaf and different vegetation types.

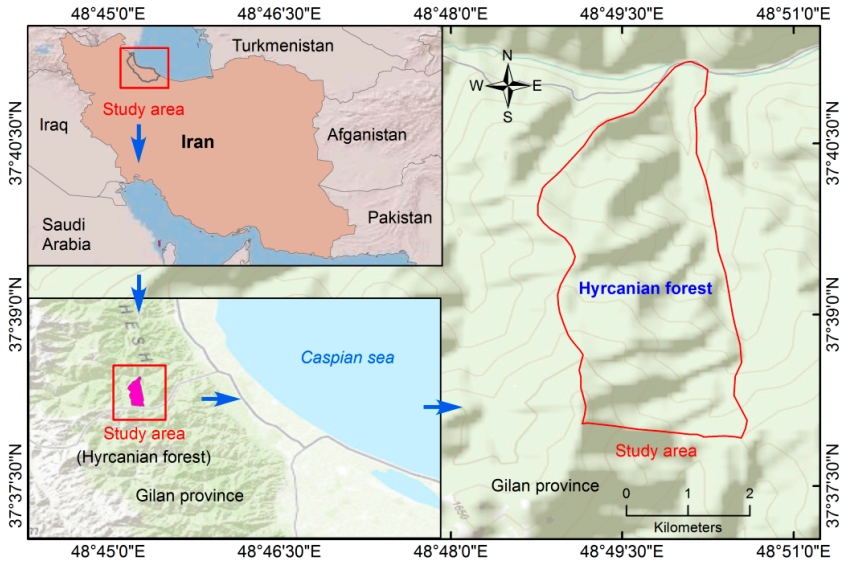

Figure 1. Location of the study area.

In this project, we selected an area of about 1100 hectares of the Hyrcanian forest for the research. This area is located between the longitudes 48°48′45″ and 48°50′35″N, and between the latitudes

37°41′13″ to 37°37′55″E. The altitude of the study area ranges from 110 m to 200 m above sea level. The forest of the study area is typically a suitable ecosystem for the broadleaf Hyrcanian species, especially *Fagus orientalis*. The forested area is natural and mature with unevenly-aged and dense to semi-dense stands. The area is comprised of mixed hardwood types such as *Fagus* dominant, mixed *Fagus*, and *Carpinus–Fagus*. The most important tree species are *Acer cappadocicum*, *Fagus orientalis*, *Carpinus Betulus*, *Tilia platyphyllos*, and *Alnus glutinosa* [34].

2.2. Data Collection and Processing

2.2.1. Satellite Data Collection and Processing

Table 1 shows the ALOS-2 PALSAR-2 L-band in full polarimetry and the Sentinel-2A MSI data used for estimating the forest AGB in this study.

Table 1. Acquired satellite remote sensing data.

Satellite	Acquisition Date	Resolution	Level	Spectral/Polarizations Used
Sentinel-2A	20 June 2016	10 m	L1C	Blue, Green, Red, NIR
ALOS-2 PALSAR-2	1 June 2015	6 m	L1.1	HH, HV, VH, VV

Source: Japan Aerospace Exploration Agency (JAXA), Japan, and European Space Agency (ESA).

The ALOS-2 PALSAR-2 data (HH, HV, VV, and VH) at level 1.1 was acquired in the dry season with almost no rainfall during the date of the acquisition (1 June 2015). The off-nadir angle (θ) is 35.3° and the range resolution is equal to 6 m (http://www.eorc.jaxa.jp/ALOS-2/en/obs/pal2_w-cycle.htm). The data was acquired in the single-look complex (SLC) format. For this research, the multi-looked method was applied for de-speckling the full-polarization ALOS-2 PALSAR-2 scene to enhance the radiometric resolution and to square the pixels in ground range geometry at a similar spatial resolution (10 m) as that of the Sentinel-2A imagery [35]. Because terrain can significantly impact the result of forest AGB estimation [12], the ALOS-2 PALSAR-2 data were radiometrically terrain-corrected and geocoded using NASA(National Aeronautics and Space Administration) 's Shuttle Radar Topography Mission Digital Elevation Model (DEM) [36]. This is suggested by JAXA [25] to correct inherent SAR geometry effects. The geocoded images were re-sampled to a regular grid with 10 m × 10 m pixel size. The intensity values were converted to the normalized radar backscattering coefficients (σ^0) using Equation (1).

$$\sigma^0[dB] = 10 \cdot log_{10}\left(I^2 + Q^2\right) + CF \quad (1)$$

where σ^0 is a backscattering coefficient; I and Q are the real and imaginary parts of the complex SAR image pixel values [25]; and CF (calibration factor) = −83 [37].

Then, the backscattering coefficients were converted into the corrected backscatter in gamma-naught (γ° values) to reduce the effect of the incidence angle on the radar backscatter. In addition, the ALOS-2 PALSAR-2 data were co-registered with the Sentinel-2A MSI scene of the study area (Table 1). In this research, we calculated additional polarimetric parameters such as the alpha angle (α), entropy (H), and anisotropy (A) for the modeling.

The Sentinel-2A MSI Level 1C data was acquired on 20 June 2016 (Table 1). The multispectral bands with spatial resolution of 10 m used are four visible bands; Blue (490 nm), Green (560 nm), Red (665 nm), and Near-Infrared (NIR) (842 nm). The Sentinel-2A Level 1C at the top of the atmosphere (TOA) reflectance data was then processed to Level-2A using ESA's Sen2Cor algorithm to obtain the bottom of the atmosphere (BOA) reflectance images using (http://step.esa.int/main/third-party-plugins-2/sen2cor/). It is noted that ENVI 5.2 software was employed for SAR imagery processing while SNAP toolbox (http://step.esa.int/main/toolboxes/snap/) was used to process the Sentinel-2A imagery.

2.2.2. Image Transformation of the Sentinel-2A MSI Data

The vegetation index is the most common image transformation for multispectral data since each index has the sensitivity for different biophysical parameters such as canopy, biomass, and volume forests. In this study, six vegetation indices including SVI (Simple Vegetation Index), RVI (Ratio Vegetation Index), NDVI (Normalized Difference Vegetation Index), EVI-2 (Enhanced Vegetation Index-2), SAVI (Soil Adjusted Vegetation Index), and PVI-2 (Perpendicular Vegetation Index-2) (see Table 2) were selected for the AGB estimation as suggested in References [31,32,38]. Additionally, Principal Component Analysis (PCA) was also computed from the four multispectral bands of the Sentinel-2A and used for the forest AGB modeling as suggested in previous studies [39,40].

Table 2. List of vegetation indices used.

Vegetation Index	Acronyms	Formula	References
Simple Vegetation Index	SVI	RED/NIR	[41]
Ratio Vegetation Index	RVI	NIR/RED	[42]
Normalized Difference Vegetation Index	NDVI	$(\mathrm{NIR}-\mathrm{RED})/(\mathrm{NIR}+\mathrm{RED})$	[43]
Enhanced Vegetation Index-2	EVI-2	$2.5(\mathrm{NIR}-\mathrm{RED})/(\mathrm{NIR}+2.4\ \mathrm{RED}+1)$	[44]
Soil Adjusted Vegetation Index	SAVI	$(1+L)\times(\mathrm{NIR}-\mathrm{RED})/(\mathrm{NIR}+2.4\ \mathrm{RED}+1)$ L = 0.5 in most conditions	[45]
Perpendicular Vegetation Index-2	PVI-2	$(IR-\alpha R+b)/\sqrt{1+a^2}$	[46]

2.2.3. Field Plot Measurement and Field Biomass Estimation

We conducted field survey measurements during the autumn of 2015 with permission from local authorities. The fieldwork did not cause any damage to the forest ecosystem. We selected these plots using a stratified random sampling in which each plot was determined based on a 200 m × 300 m grid overlaid over the entire territory to ensure the range of biomass values. A total of 149 sampling plots with a plot size of 30 × 30 m^2 were measured for specific biophysical parameters such as the diameter at breast height (DBH) and tree height. All trees with DBH greater than 7.5 cm were measured. The DBH and the tree height were measured with pulse-laser technology. The center location of each plot was recorded using the Trimble R3 differential global positioning system (DGPS). The four corners of each sampling plot were established in the field using the DGPS method with a plot size of 30 m × 30 m. This allowed for access to the ALOS-2 PALSAR-2 with a pixel size of 6 × 6 m^2, and the Sentinel-2A with a pixel size of 10 × 10 m^2. To minimize the positional inaccuracies of DGPS and geo-coding, we calculated the mean of the pixel for each sampling plot with a moving window size of 3 × 3 pixels for the Sentinel-2A and a window size of 3 × 3 pixels for the ALOS-2 PALSAR-2 data.

Because there is no specific allometric equation for the Hyrcanian forest types, we calculated the forest AGB of each tree using the specific gravity method for different forest species of the study area. For this purpose, we first calculated a tree volume based on the standard volume table, and then converted it to biomass using the specific gravity of each species. Finally, the forest AGB of each plot was calculated. Once the forest AGB was calculated in each plot, we summed up all of the AGB values and converted them to $Mg{\cdot}ha^{-1}$.

Table 3 shows the field data of measured AGB in the sample plots in the study area. The forest AGB in the study area ranged between 45.67 and 436.17 $Mg{\cdot}ha^{-1}$ and had an average of 206.54 $Mg{\cdot}ha^{-1}$.

Table 3. Characteristics of the forest aboveground biomass (AGB) in the study area.

Attribute	Minimum ($Mg{\cdot}ha^{-1}$)	Maximum ($Mg{\cdot}ha^{-1}$)	Mean ($Mg{\cdot}ha^{-1}$)	Standard Deviation ($Mg{\cdot}ha^{-1}$)
AGB (n = 149)	45.67	436.17	206.54	78.01

2.2.4. Generation of the Training Dataset and the Validation Dataset

We randomly split the 149 sample plots into two subsets, with the first one (120 sample plots or 80%) used for training models and the second one (29 sample plots or 20%) used for model validation and confirming the prediction accuracy. It is noted that the forest AGBs from the sample plots were used as the dependent variable, whereas the independent variables were derived from the Sentinel-2A data and the ALOS-2 PALSAR-2 data. In the next step, three datasets were generated: (1) the Sentinel-2A dataset; (2) the ALOS-2 PALSAR-2 dataset; and the combination of the Sentinel-2A dataset and the ALOS-2 PALSAR-2 dataset (Sentinel-ALOS). A summary of these datasets is shown in Table 4. All the explanation variables were normalized for use in the machine learning models.

Table 4. Description of the three datasets used in the forest AGB estimation in the study area.

No.	Name	Explanation Variable
1	The Sentinel-2A dataset	Blue band, Green band, Red band, NIR band, SVI, RVI, NDVI, EVI, SAVI, PVI-2, PCA1, PCA2, and PCA3
2	The ALOS-2 PALSAR-2 dataset	HH, HV, VH, VV, HH-HV, Anisotropy, Alpha, and Entropy
3	The Sentinel-ALOS dataset (Combination of the Sentinel-2A dataset and the ALOS-2 PALSAR-2 dataset)	Blue band, Green band, Red band, NIR band, SVI, RVI, NDVI, EVI, SAVI, PVI-2, PCA1, PCA2, PCA3, HH, HV, VH, VV, HH-HV, Anisotropy, Alpha, and Entropy

3. Theoretical Background of the Method Used

3.1. Random Forest

Random Forest (RF) is an efficient machine learning method proposed by Breiman [47] that can be used both for classification and regression purposes. RF has proven to yield high accuracy, find the robust outliers and noise, compute quickly, and show the relative importance of input variables [48,49].

In RF, the bagging (bootstrap aggregating) algorithm [50] is used to generate n sub-datasets from the training dataset. These sub-datasets are called bootstrap datasets. Each bootstrap dataset is used to constructed a base-decision tree using the Classification And Regression Tree (CART) algorithm [51]. Finally, these base-decision trees are grouped to form a forest called the RF model.

Ideally, two-thirds of the total samples from the training dataset should be included in these bootstrap datasets and called 'in bag' data. The remaining data is called 'out-of-bag' (OOB) data, and is used to evaluate the RF model [52].

Because the performance of the RF model is dependent on the number of the base-decision trees used, this parameter should be carefully selected. For this research, 500 base-decision trees were selected to ensure the diversity of the random forest model as suggested in [53,54].

3.2. Support Vector Regression

Support Vector Regression (SVR) is one of the most efficient machine learning techniques developed, according to the statistical learning theory [55,56]. SVR has proven to outperform conventional methods in environmental modeling [57–61], land-use and land-cover classification [62], and estimating forest biomass [32,63]. The main advantage of SVR is that it is highly accurate at predicting even with small numbers of training samples [64].

For the forest AGB estimation, the training process aims to build an SVR function as follows:

$$\mathrm{AGB} = \sum_{i=1}^{n} \alpha_i k(x_i;\ x) + b \tag{2}$$

where $k\,(x_i; x)$ represents the kernel function; x_i is the training vector; α denotes the Lagrange multiplier; and b is the bias term in the regression.

The quality of the forest AGB estimation is measured by the ε-insensitive loss function proposed by Vapnik [65]. In addition, the performance of the SVR model is significantly influenced by

the selection of the kernel functions. Therefore, in this research, we selected the Radial Basis Function (RBF) kernel because it is the most widely used for determining forest biomass in previous studies [31,32,63]. Consequently, the training of the SVR model required finding the best values for the two meta-parameters, the regularization parameter (C), and the kernel width (γ). For this task, the grid search method was used, as seen in Reference [66,67]. Accordingly, the SVR model was constructed using the best C = 18 and γ = 0.102 for the SVR model with the Sentinel-2A dataset, while the best C = 17 and γ = 0.102 were found for the ALOS-2 PALSAR-2 dataset. For the Sentinel-ALOS dataset, C = 6 and γ = 0.102 are the best values.

3.3. Multi-Layer Perceptron Neural Network

An artificial neural network consists of a large number of highly interconnected nodes using mathematical algorithms to model non-linear complex problems such as forest biomass modeling. Although various neural network algorithms have been developed, multi-layer perceptron neural networks (MLP Neural Nets) are the most widely used for environmental modeling [68,69], forest monitoring and mapping [70], and forest biomass estimation [71]. The structure of a typical MLP Neural Nets model consists of three layers including input, hidden, and output layers, where each layer is composed of several nodes or neurons. In the input layer, the number of neurons represents the number of input explanatory variables, while the number of neurons in the hidden layer must be determined beforehand depending on the data of the study area. The output layer contains one neuron, which indicates the values of the forest AGB in this study.

The performance of the MLP Neural Nets model is significantly affected by connection weights between the input and hidden layers and between the hidden and the output layers. These weights are adjusted and modified accordingly in the training phase based on a back-propagation algorithm [72] meant to minimize the difference between the AGB value generated from the MLP Neural Nets model and the forest AGB inventories. The process is repeated until a predefined accuracy level or the maximum number of repetitions is reached.

To construct the MLP Neural Nets model for this study, the number of hidden neurons that has a significant impact on the forest AGB estimation [71,73] was determined using the test suggested in Reference [58]. Thus, by varying the numbers of neurons versus the root-mean-square error (RMSE) using the training dataset, the best MLP Neural Nets models were determined for the three datasets in this study. These best models are characterized by the highest R^2, the lowest RMSE, and the lowest MAE (mean absolute error). Accordingly, the best MLP Neural Nets model with two neurons was found for the Sentinel-2A dataset, while three neurons were found for the ALOS-2 PALSAR-2 dataset and four neurons were found for the combination Sentinel-ALOS dataset. The activation function of the logistic sigmoid was used. The learning rate, momentum, and training iteration were selected as 0.3, 0.2, and 500, respectively, as suggested in Reference [74,75].

3.4. Gaussian Processes

Gaussian process (GP) is considered a powerful regression method that has successfully been used in various real world problems [76,77], including calculating aboveground forest biomass [78]. GP is a stochastic process that regresses probability distribution functions over the forest AGB data under the assumption that these functions have a Gaussian distribution.

In the GP regression model, a relation between the input variables $x_i = [x_1, \ldots, x^B] \in R^B$ and the output AGB $y \in R$ could be expressed by the following equation:

$$\hat{y} = f(x) = \sum_{i=1}^{n} \alpha_i K(x_i, x) \tag{3}$$

where x_i is the explanatory variables used in the training phase; α_i is the weight assigned to each one of them; and K is a kernel function [79,80].

A GP assumes that $p(f(x_1), \ldots, f(x_N))$ is jointly Gaussian, with some mean $\mu(x)$ and covariance $\Sigma(x)$ given by $\Sigma_{ij} = k(x_i, x_j)$, with k representing a kernel function.

A scaled Gaussian kernel function was employed, using the following equation:

$$K(x_i, x_j) = v \exp\left(-\sum_{b=1}^{B}\left(x_i^{(b)} - x_j^{(b)}\right)^2/(2\sigma_b^2)\right) \quad (4)$$

where v is a scaling factor, B is the number of input explanatory variables, and σ_b is a dedicated parameter controlling the spread of the relations for each particular input variable b. Model parameters (v, σ_b) and model weights α_i can be automatically optimized by maximizing the marginal likelihood in the training set [76,81].

3.5. Model Assessment

Models generated from machine learning techniques were validated using the field survey data. A total of 29 sample plots (20% of plots) was randomly selected to assess the performance of these models (as described in Section 2.2.4), of which the forest AGB ranged from 89.74 to 382.15 Mg·ha^{-1}.

We used the root-mean-square-error (RMSE), the mean absolute error (MAE), and the coefficient of determination (R^2) to compare the performance of selected machine learning techniques for the forest AGB estimation. These statistical criteria are widely employed in modeling forest biomass to assess the difference between the observed data and the predicted forest AGB data [82,83].

RMSE (Equation (5)) is considered a standard metric for measuring errors of regression models. However, the equation is significantly influenced by large values and outliers [84]. Therefore, MAE (Equation (6)) is used with RMSE for evaluating the variation of the model errors [58]. Lower RMSE and MAE values indicate the better regression model. Furthermore, a smaller difference between RMSE and MAE reflects a smaller variance between the errors. R^2 is estimated using Equation (7); and the higher the R^2 values also show a better model [68,71,85].

$$\text{RMSE} = \sqrt{\sum_{i=1}^{n}\frac{(\hat{y}_i - y_i)^2}{n}} \quad (5)$$

$$\text{MAE} = \frac{1}{n}\sum_{i=1}^{n}|\hat{y}_i - y_i| \quad (6)$$

$$R^2 = 1 - \frac{\sum_{i=1}^{n}(y_i - \hat{y}_i)^2}{\sum_{i=1}^{n}(y_i - \bar{y})^2} \quad (7)$$

where $\hat{y}_i$ and y_i are the predicted and observed biomass for the ith plot, respectively; n is the total number of validation plots, and $\bar{y}$ is the observed mean values of biomass.

4. Result and Analysis

4.1. Model Training and Validation

The results of the forest AGB estimation using RF, SVR, MLP Neural Nets, and GP models for the Sentinel-2A dataset are shown in Table 5. The results show that all four models had satisfactory performances using the training data. The highest goodness of fit was found for the RF model (R^2 = 0.95, RMSE = 20.35, MAE = 3.54), followed by the SVR model (R^2 = 0.74, RMSE = 40.55, MAE = 23.99), the MLP Neural Nets model (R^2 = 0.72, RMSE = 43.80, MAE = 31.57), and the GP model (R^2 = 0.70, RMSE = 44.32, MAE = 30.88). In addition, the SVR model yielded the highest performance when using the validation data (R^2 = 0.68, RMSE = 42.04, MAE = 36.53), and was followed by the GF model (R^2 = 0.70, RMSE = 46.71, MAE = 39.81). In contrast, the MLP Neural Nets model had the lowest performance (R^2 = 0.58, RMSE = 47.39, MAE = 37.31).

Table 5. Training and validation results of the AGB model using the Sentinel-2A dataset.

AGB Model	Training Dataset			Validation Dataset		
	R^2	RMSE	MAE	R^2	RMSE	MAE
RF	0.95	20.35	3.54	0.62	45.00	37.59
SVR	0.74	40.55	25.99	0.68	42.04	36.53
MLP Neural Nets	0.72	43.80	31.57	0.58	47.39	37.31
GP	0.70	44.32	30.88	0.70	46.71	39.81

Analysis of the R^2 values for the AGB estimation models using the ALOS-2 PALSAR-2 data in Table 6 indicates that most values ranged from 0.37 to 0.55 for the training data and ranged from 0.13 to 0.23 for the validation data, apart from the RF model for the training data. Overall, the ALOS-2 PALSAR-2 imagery had a very weak correlation with the AGB estimation. Considering the existing reports on the saturation of SAR backscatter data at a high level of AGB, one could expect such weak relationships, especially for high biomass tropical forests. The ALOS-2 PALSAR-2 data alone led to very poor modeling of the forest AGB in the study area.

It is clearly seen from Table 7 that, among the four machine learning models, the SVR model had the highest performance with the Sentinel-ALOS dataset (both on the training and the validation datasets). This shows a strong relationship between the observed and predicted AGB values, where R^2, RMSE, and MAE were 0.86, 38.66 Mg·ha^{-1}, and 20.19 Mg·ha^{-1} on the training dataset and 0.73, 38.68 Mg·ha^{-1}, and 32.28 Mg·ha^{-1} on the validation dataset, respectively. In addition, MAE values were clearly lower than RMSE values, which indicates that the model has a low variance of the individual errors in the two datasets. In contrast to the SVR model, the MLP Neural Nets model had the lowest performance: R^2, RMSE, and MAE on the training dataset and on the validation dataset were 0.87, 34.98 Mg·ha^{-1}, and 25.71 Mg·ha^{-1} and 0.44, 64.33 Mg·ha^{-1}, and 53.74 Mg·ha^{-1}, respectively.

Table 6. Training and validation results of the AGB model using the ALOS-2 PALSAR-2 dataset.

AGB Model	Training Dataset			Validation Dataset		
	R^2	RMSE	MAE	R^2	RMSE	MAE
RF	0.95	26.48	5.91	0.12	65.43	58.20
SVR	0.51	60.89	44.35	0.16	64.04	52.86
MLP Neural Nets	0.55	57.17	43.48	0.13	66.34	52.76
GP	0.37	70.74	56.84	0.23	64.67	51.98

Table 7. Training and validation results of the AGB model using the combination of the Sentinel-2A dataset and the ALOS-2 PALSAR-2 dataset (Sentinel-ALOS).

AGB Model	Training Dataset			Validation Dataset		
	R^2	RMSE	MAE	R^2	RMSE	MAE
RF	0.97	19.41	2.96	0.62	43.13	35.83
SVR	0.86	38.66	20.19	0.73	38.68	32.28
MLP Neural Nets	0.87	34.98	25.71	0.44	64.33	53.74
GP	0.80	44.48	29.82	0.69	40.11	33.69

Compared to the results from the Sentinel-2A MSI and the ALOS-2 PALSAR-2 images, their combination significantly improved the performance of the SVR model, but the data integration did not improve the model performances in terms of R^2, RMSE, and MAE values for the other machine learning techniques. Overall, the MLP Neural Nets and the GP models had lower R^2 values and higher RMSE and MAE values. Therefore, we conclude that the SVR model achieved the best performance for estimating the forest AGB in this study.

As can be seen from Table 7, the SVR model achieved the highest R^2 value and the lowest RMSE and MAE values among the four machine learning models. The GP model had a lower error rate than the RF and MLP Neural Nets models. This is likely due to the saturation levels at 274.42 Mg·ha^{-1}.

4.2. Accuracy Assessment of Aboveground Biomass

Figure 2 shows scatterplots of predicted versus observed AGB to show the accuracy of the estimated forest AGB by different machine learning techniques at the study site. As can be seen, the highest saturation level was observed by the SVR model exceeding 237.40 Mg·ha^{-1}. Although the MLP Neural Nets model showed a higher value, it should be noted that this model has a random behavior in the biomass estimation.

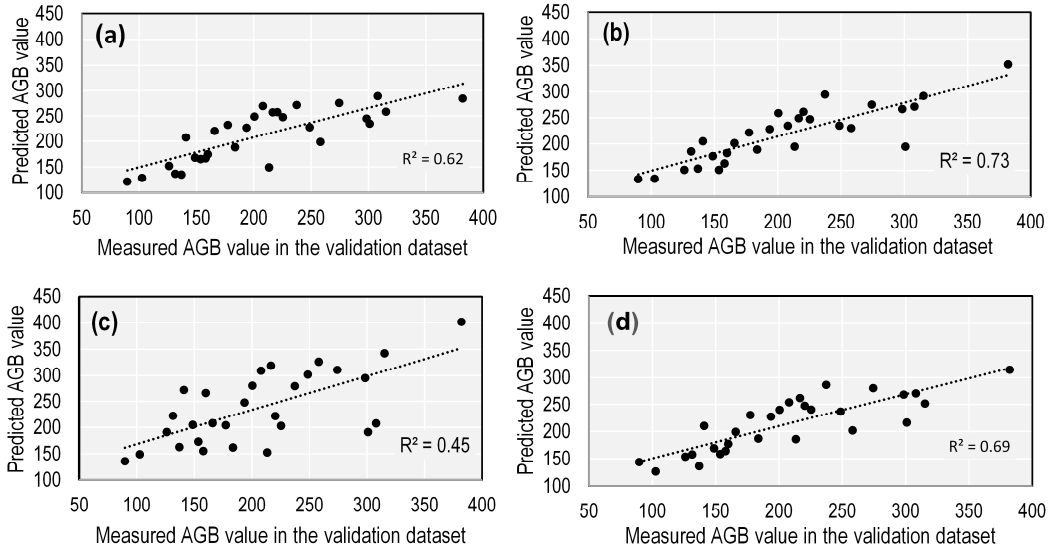

Figure 2. Comparison between the measured AGB in the Sentinel-ALOS validation dataset and the predicted forest AGB using: (**a**) the RF model; (**b**) the SVR model: (**c**) the MLP Neural Nets model; and (**d**) the GP model.

The comparison of the behavior between the four different machine learning models used in biomass estimation is shown in Figure 3. The results revealed that the predicted AGB by the SVR model is consistent with observed AGB. However, the actual biomass value before 237.40 Mg·ha^{-1} is likely overestimated, and after 248.0 Mg·ha^{-1}, all models are underestimated and reach their saturation level. The biomass of plots containing dense large forest stands with high DBH were likely underestimated due to the saturation levels of the ALOS-2 PALSAR-2 and the Sentinel-2A sensors for estimating forest AGB.

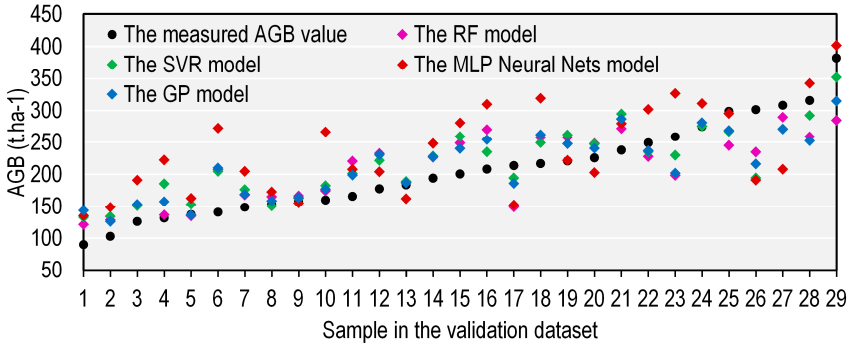

Figure 3. Comparison of the predicted AGB and the measured AGB values.

All machine learning models, apart from the MLP Neural Nets model, have the ability to estimate AGB exceeding 183.75 Mg·ha^{-1}. In this range, the SVR model has a better performance than the other models. Therefore, the model was selected for estimating the forest AGB in this study. The results were converted to a raster format to open in ArcGIS 10.3 software. The AGB map was visualized by eight classes (Figure 4) showing a range from 50.2 to 467.2 Mg·ha^{-1} (average = 226.9 Mg·ha^{-1}).

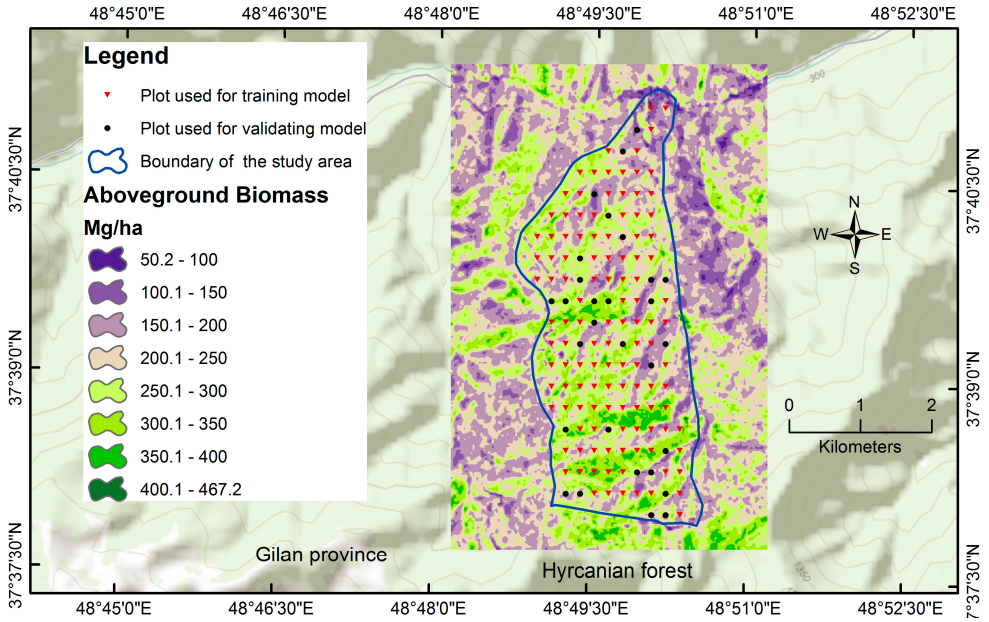

Figure 4. The AGB generated from the SVR model in the study area.

The relationships between the plot-measured AGB, spectral bands, and vegetation indices derived from the Sentinel-2A data were further analyzed and presented in scatterplots in Figure 5. It could be seen that RVI had the highest correlation coefficient (R^2 = 0.519) with the plot-measured AGB, followed by NDVI (R^2 = 0.507), PCA1 (R^2 = 0.502), SVI (R^2 = 0.500), PVI-2 (R^2 = 0.462), NIR (R^2 = 0.396), Red band ((R^2 = 0.367), EVI (R^2 = 0.354), PCA3 (R^2 =0.266), SAVI (R^2 = 0.232), PCA2 (R^2 = 0.207), Green band (R^2 = 0.183), and Blue band (R^2 = 0.153).

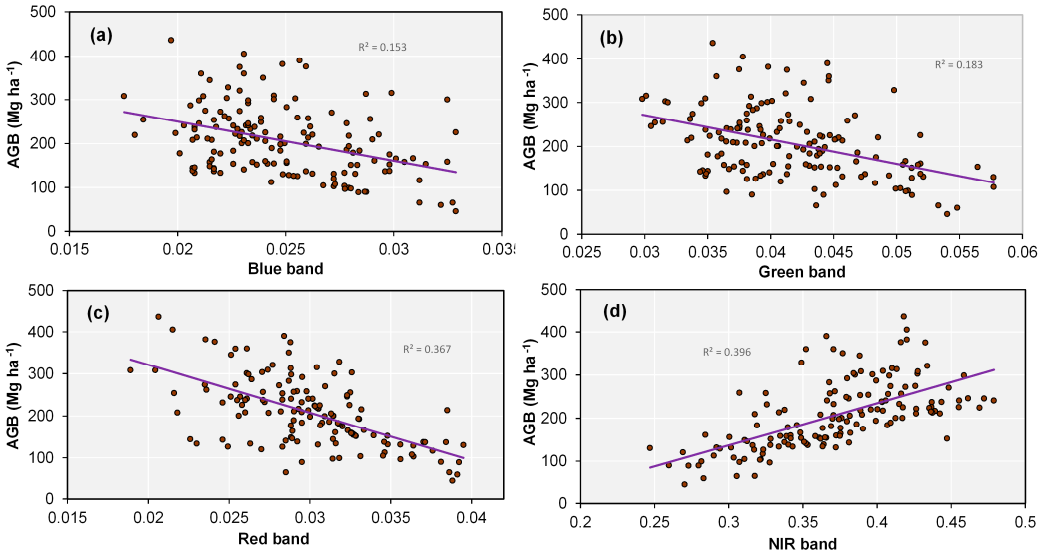

Figure 5. *Cont.*

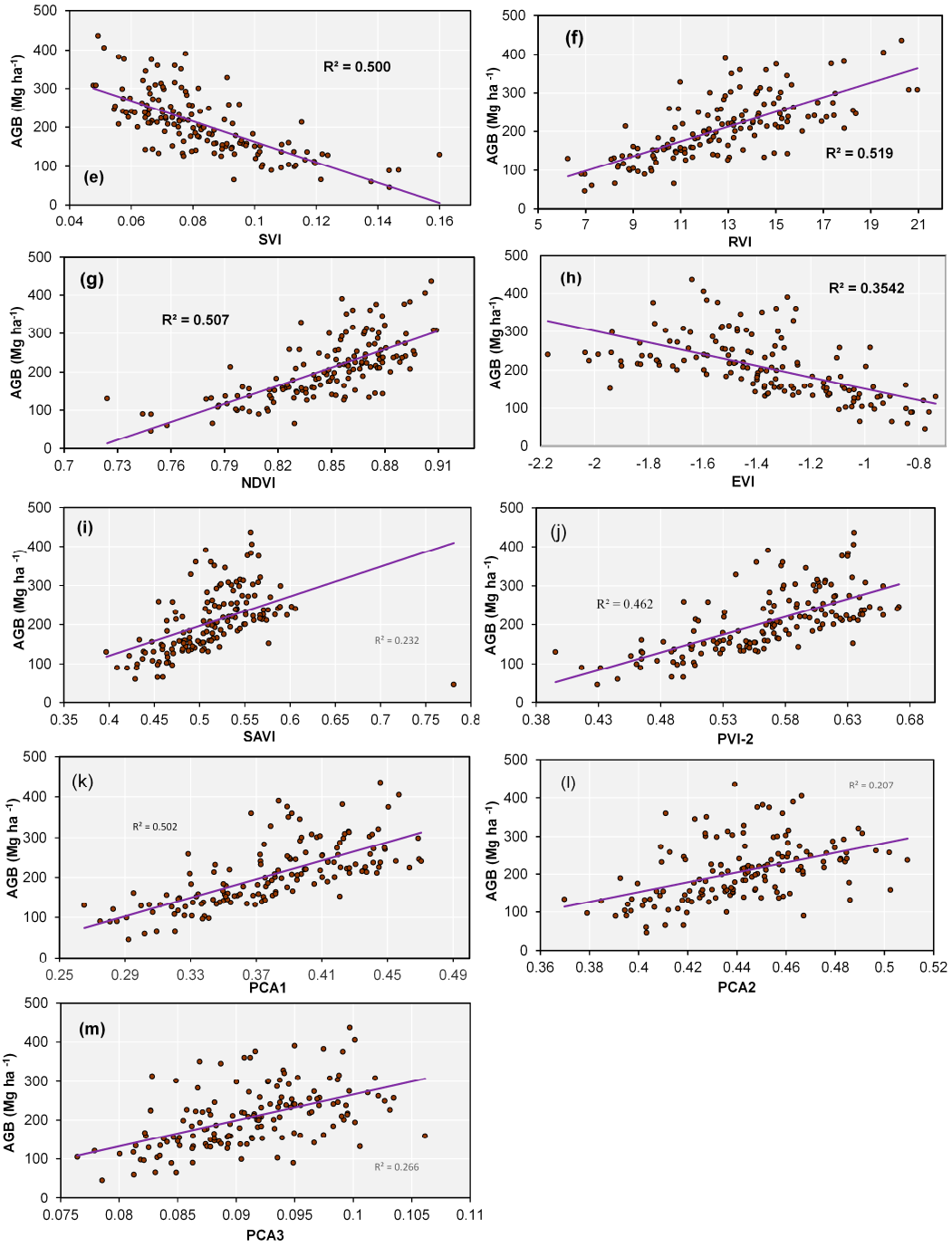

Figure 5. The AGB (Mg·ha^{-1}) versus 13 variables derived from the Sentinel-2A for the study area: (**a**) AGB versus Blue band; (**b**) AGB versus Green band; (**c**) AGB versus Red band; (**d**) AGB versus NIR band; (**e**) AGB versus SVI; (**f**) AGB versus RVI; (**g**) AGB versus NDVI; (**h**) AGB versus EVI; (**i**) AGB versus SAVI; (**j**) AGB versus PVI-2; (**k**) AGB versus PCA1; (**l**) AGB versus PCA2; and (**m**) AGB versus PCA3.

The relationships between the plot-measured AGB and the eight factors derived from the ALOS-2 PALSAR-2 data are shown in Figure 6. It can be seen that HV had the highest correlation coefficient (R^2 = 0.182) with the plot-measured AGB, followed by HH-HV (R^2 = 0.113), VV (R^2 = 0.069), Entropy (R^2 = 0.018), VH (R^2 = 0.002), Alpha (R^2 = 0.002), HH (R^2 = 0.001), and Anisotropy (R^2 = 0.001). These indicate weak correlations between these variables and the plot-measured AGB. Therefore, using the variables

derived from the ALOS-2 PALSAR-2 alone led to very poor results of the forest AGB estimation in the study area.

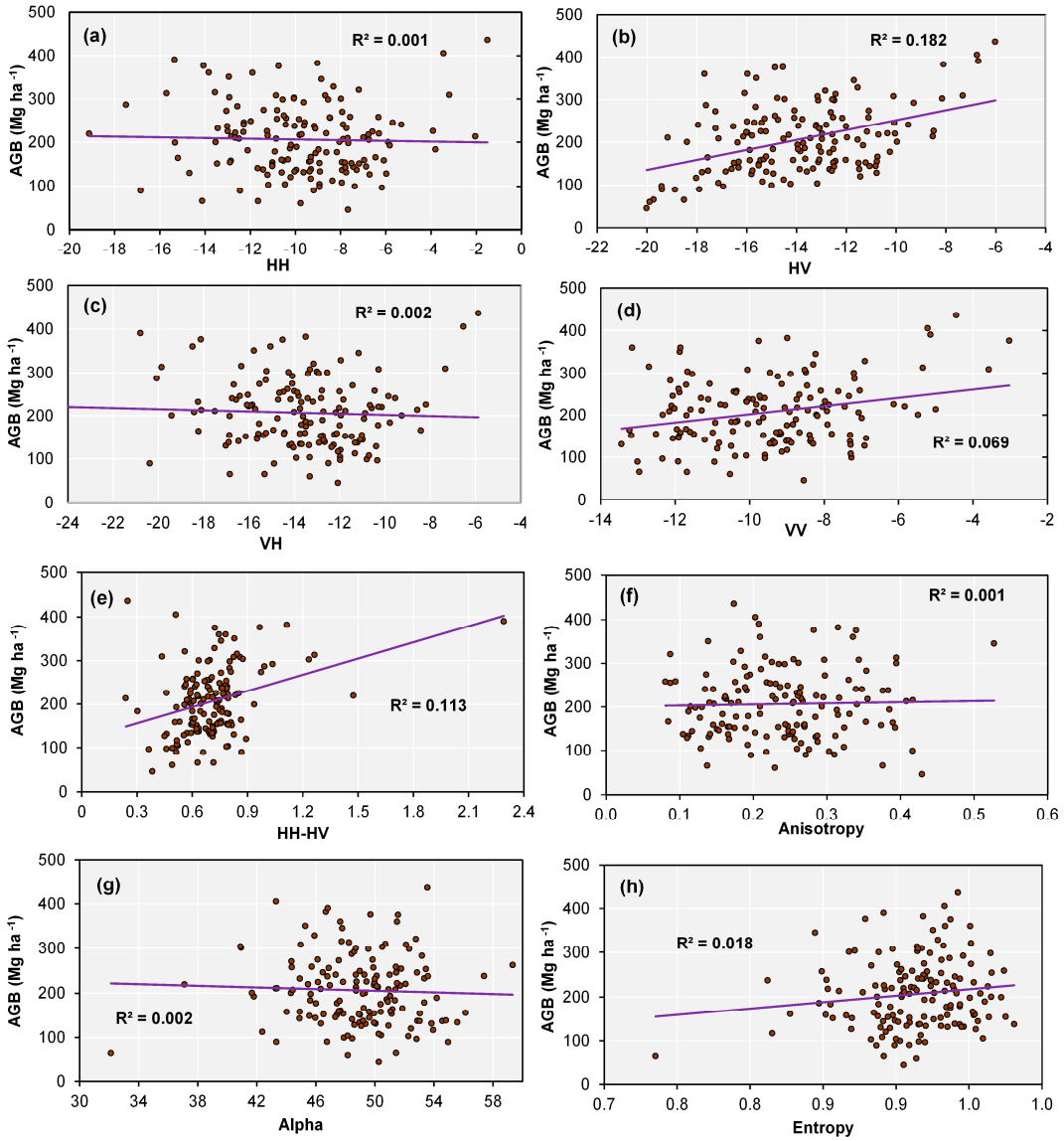

Figure 6. The AGB (Mg·ha^{-1}) versus eight variables derived from the Sentinel-2A for the study area: (**a**) AGB versus HH; (**b**) AGB versus HV; (**c**) AGB versus VH; (**d**) AGB versus VV; (**e**) AGB versus HH-HV; (**f**) AGB versus Anisotropy; (**g**) AGB versus Alpha; and (**h**) AGB versus Entropy.

4.3. The Role of the Predictive Variables

The role of the predictive variables for the AGB estimation in this study was assessed using RF with the wrapper evaluation method [86,87] that is available in the Weka software. Accordingly, the correlation coefficient was used to calculate the merit of the variables. The result is shown in Table 8.

It can be seen that SVI, NDVI, and RVI, derived from the multispectral bands of the Sentinel-2A data, were the most important variables for predicting the forest AGB in the study area. This is likely due to the strong correlation coefficients between the forest AGB and SVI, NDVI, and RVI, which are consistent with the results from the scatterplots (Figure 5). The result was in line with recent study results reported in Shen et al. [88] and Pargal et al. [89]. Our results suggest that SVI, NDVI, RVI, and PCA1 generated from Sentinel-2A data play an important role in the forest AGB estimation compared to other vegetation indices in the study area. The results were similar to findings [90] and

Patel and Majumdar [39]. Table 8 also shows that PCA1 and PCA3, derived from multispectral bands, were important variables for predicting the forest AGB. A similar finding was made by Lu et al. [91] and Patel and Majumdar [39]. In contrast, Entropy and Alpha derived from the ALOS-2 PALSAR-2 dataset presented low contributions to the estimation of the forest AGB in this study.

Table 8. The importance of the variables for the AGB estimation in this study measured using RF with the wrapper evaluation method.

Merit Value	Variable	Ranking
0.730	SVI	1
0.729	NDVI	2
0.727	RVI	3
0.716	PCA1	4
0.703	PCA3	5
0.697	SAVI	6
0.682	EVI	7
0.621	PVI-2	8
0.607	NIR	9
0.571	Red	10
0.511	HV	11
0.49	Blue	12
0.457	VV	13
0.437	VH	14
0.412	PCA2	15
0.401	Green	16
0.303	HH-HV	17
0.293	HH	18
0.268	Anisotropy	19
0.183	Alpha	20
0.130	Entropy	21

5. Discussion

The use of satellite remote sensing data for estimating the forest AGB is still challenging in semitropical and mountainous areas due to numerous factors influencing the relationship between AGB and remote sensing variables. The challenging factors include topography, soil conditions, and forest structures [20]. Therefore, investigating new remotely sensed data, including their fusions and combinations, for forest AGB estimation is very necessary. This study addresses key issues by investigating the combination of remote sensing data of the Sentinel-2A and the ALOS-2 PALSAR-2 for estimating the forest AGB. However, the combinations of optical images (i.e., Landsat) and SAR images (i.e., JERS-1 SAR) for the forest AGB estimation are not new [21]. Yet, to the best of our knowledge, investigating the combination of the Sentinel-2A and the ALOS-2 PALSAR-2 for the estimation of forest ABG has seldom been carried out. This may be due to the new launch of the Sentinel-2A (23 June 2015) and the ALOS-2 PALSAR-2 (24 May 2014). In addition, four current state-of-the art machine learning methods (RF, SVR, MLP Neural Net, and GP) were considered in this research for comparing and selecting the best model. The selection of the prediction method is key and does have a significant effect on the estimation accuracy [78]. Furthermore, R^2 RMSE and MAE were used to assess the quality of the forest AGB models.

The results of this study indicate that the combination of the Sentinel-2A data and the ALOS-2 PALSAR-2 data significantly improved the estimation accuracy of the forest AGB. This finding is consistent with the conclusions of previous studies, where they pointed out that combining optical (Landsat TM, SPOT) and SAR images (JERS-1 and ERS-1/2) can improve the accuracy of estimating AGB [23].

Among the four machine learning models, the SVR model provided the highest estimation accuracy in terms of the highest R^2, the lowest RMSE, and the lowest MAE. It was followed by the

GP model, the RF model, and the MLP Neural Net model. These results are reasonable because the SVR model has proven robust and efficient with small datasets [92,93]. This result is in agreement with the findings reported in References [94–97], which concluded that SVR consistently outperformed other machine learning methods. The performance (R^2 of 0.73 and RMSE of 38.68 Mg·ha^{-1}, Table 7) of the SVR model with the combination data of the Sentinel-2A and the ALOS-2 PALSAR-2 indicates a satisfactory result compared to previous studies on the forest AGB, as seen in Reference [98] (R^2 = 0.46), (R^2 = 0.28–0.44) [21], and (R^2 = 0.46) [99].

When considering the use of the Sentinel-2A dataset only, all of the models show moderate prediction performance (R^2 = 0.58–0.70). However, the SVR model has the highest prediction accuracy (R^2 = 0.68, RMSE = 42.04 Mg·ha^{-1}, and MAE = 36.53 Mg·ha^{-1}). This is due to the Sentinel-2A sensor providing high spatial resolution of images (10 m) and due to the correlation of the Sentinel-2A with the AGB of the study area being significant. In contrast, the four models all showed very low performance (R^2 = 0.12–0.23) with the ALOS-2 PALSAR-2 data. The models only indicated that the ALOS-2 PALSAR-2 data have a weak correlation with the AGB of the study area. This finding is different compared to those reported by Ghasemi, Sahebi and Mohammadzadeh [14] (R^2 = 0.61) and Attarchi and Gloaguen [12] (R^2 = 0.45). However, they used the ALOS PALSAR data. The reason for the difference may be due to the wavelength transformations used for preprocessing the ALOS PALSAR images in Reference [90] and the ALOS PALSAR textures being used in Reference [12] that have improved the performance of their models.

We found that that SVI, NDVI, and RVI generated from Sentinel-2A data played an important role in the AGB estimation of the study area. In addition, PCA1 was more important in AGB estimation than PVI-2. A further in-depth study is highly recommended to improve the understanding of the significance of image transformation such as vegetation indices derived from other spectral bands of Sentinel-2A data in AGB estimation.

One of the critical problems in estimating the forest AGB is data saturations, which often cause low accuracy for estimating the AGB in high biomass or high canopy density areas. It should be noted that a short wavelength such as the C-band at 6 cm saturates often at 10 kg/m^2, while long wavelengths such as the L-band saturate often at 100 Mg ha^{-1} in complex and mixed forest structures. This saturation number rises to roughly 250 Mg·ha^{-1} for simple forests with a few dominant species [100]. The saturation level of the ALOS-2 PALSAR-2 sensor for AGB estimation, reported by our previous studies, is around 100–150 Mg·ha^{-1} [71]. The problem surrounding the data saturation could be partly solved through the use of multi-source data or data fusion [101,102]. Thus, the result in this study indicates that the integration of the Sentinel-2A data and the ALOS-2 PALSAR-2 data reduced the saturation problem. Consequently, the SVR model developed in this study has the ability to estimate biomass AGB exceeding 237.40 Mg·ha^{-1}.

The main limitation of the current work is the lack of standard allometric equations for estimating the forest AGB. In fact, a large variation in stand-level AGB estimation has been observed [103]. Thus, in this work, the amount of AGB in the sample plots was calculated using the reported specified gravity for each species only. In addition, only four machine learning methods, namely RF, SVR, MLP Neural Net, and GP, were investigated. Therefore, the accuracy of the forest AGB estimation may be enhanced if other newer machine learning algorithms are used. Furthermore, for the SVR model, the best regularization parameter (C) and the kernel width (γ) were determined by the grid search method, which may not guarantee that the optimal values were found. Thus, new meta-heuristic machine learning optimization techniques should be further considered to improve the performance of the forest AGB model.

Despite the limitations, the results in this study indicate that combining the Sentinel-2A data, the ALOS-2 PALSAR-2 data, and machine learning is effective for forest biomass modeling that supports the REDD+ mechanism in developing countries.

6. Conclusions

This study investigated the potential use of data integration of the Sentinel-2A and the ALOS-2 PALSAR-2 for estimating the forest AGB of the Hyrcanian forest (Iran). In addition, four state-of-the art machine learning methods, including RF, SVR, MLP Neural Net, and GP, were investigated and compared. Based on the finding in this research, the following conclusions are drawn:

- The integration of the ALOS-2 PALSAR-2 and the Sentinel-2A data can improve the estimation accuracy of the forest AGB.
- SVR is capable of delivering the highest prediction accuracy of the forest AGB compared to RF, MLP Neural Net, and GP.
- The Sentinel-2A data could be used to estimate the forest AGB with moderate accuracy, while the ALOS-2 PALSAR-2 data alone is not enough for estimating the forest AGB.
- The results of the current work may accommodate provincial decision-making on sustainable forest monitoring and management.

Acknowledgments: This research was funded by Lorestan University, Iran. The data analysis and write-up were carried out as a part of the first author's PhD studies at the Faculty of Agriculture and Natural Resources, Lorestan University, Khoram Abad, Iran.

Author Contributions: Sasan Vafaei, Javad Soosani, Kamran Adeli, Hadi Fadaei, and Hamed Naghavi collected, processed, and interpreted the data. Dieu Tien Bui, Sasan Vafaei, Javad Soosani, and Tien Dat Pham designed the analysis, constructed models, and wrote the manuscript.

Conflicts of Interest: The authors declare no conflicts of interest.

References

1. Qureshi, A.; Pariva; Badola, R.; Hussain, S.A. A review of protocols used for assessment of carbon stock in forested landscapes. *Environ. Sci. Policy* **2012**, *16*, 81–89. [CrossRef]
2. Pham, L.T.H.; Brabyn, L. Monitoring mangrove biomass change in vietnam using spot images and an object-based approach combined with machine learning algorithms. *ISPRS J. Photogramm. Remote Sens.* **2017**, *128*, 86–97. [CrossRef]
3. Solberg, S.; Hansen, E.H.; Gobakken, T.; Næssset, E.; Zahabu, E. Biomass and insar height relationship in a dense tropical forest. *Remote Sens. Environ.* **2017**, *192*, 166–175. [CrossRef]
4. Hansen, M.C.; Potapov, P.V.; Moore, R.; Hancher, M.; Turubanova, S.A.; Tyukavina, A.; Thau, D.; Stehman, S.V.; Goetz, S.J.; Loveland, T.R.; et al. High-resolution global maps of 21st-century forest cover change. *Science* **2013**, *342*, 850–853. [CrossRef] [PubMed]
5. Steininger, M.K. Satellite estimation of tropical secondary forest above-ground biomass: Data from brazil and bolivia. *Int. J. Remote Sens.* **2000**, *21*, 1139–1157. [CrossRef]
6. Mitchard, E.T.A.; Feldpausch, T.R.; Brienen, R.J.W.; Lopez-Gonzalez, G.; Monteagudo, A.; Baker, T.R.; Lewis, S.L.; Lloyd, J.; Quesada, C.A.; Gloor, M.; et al. Markedly divergent estimates of amazon forest carbon density from ground plots and satellites. *Glob. Ecol. Biogeogr.* **2014**, *23*, 935–946. [CrossRef] [PubMed]
7. Nordh, N.-E.; Verwijst, T. Above-ground biomass assessments and first cutting cycle production in willow (*Salix* sp.) coppice—A comparison between destructive and non-destructive methods. *Biomass Bioenergy* **2004**, *27*, 1–8. [CrossRef]
8. Zolkos, S.G.; Goetz, S.J.; Dubayah, R. A meta-analysis of terrestrial aboveground biomass estimation using lidar remote sensing. *Remote Sens. Environ.* **2013**, *128*, 289–298. [CrossRef]
9. Næsset, E.; Ørka, H.O.; Solberg, S.; Bollandsås, O.M.; Hansen, E.H.; Mauya, E.; Zahabu, E.; Malimbwi, R.; Chamuya, N.; Olsson, H.; et al. Mapping and estimating forest area and aboveground biomass in miombo woodlands in tanzania using data from airborne laser scanning, tandem-x, rapideye, and global forest maps: A comparison of estimated precision. *Remote Sens. Environ.* **2016**, *175*, 282–300. [CrossRef]
10. Fayad, I.; Baghdadi, N.; Guitet, S.; Bailly, J.-S.; Hérault, B.; Gond, V.; El Hajj, M.; Tong Minh, D.H. Aboveground biomass mapping in french guiana by combining remote sensing, forest inventories and environmental data. *Int. J. Appl. Earth Obs. Geoinf.* **2016**, *52*, 502–514. [CrossRef]

11. Hyyppä, J.; Hyyppä, H.; Inkinen, M.; Engdahl, M.; Linko, S.; Zhu, Y.-H. Accuracy comparison of various remote sensing data sources in the retrieval of forest stand attributes. *Forest Ecol. Manag.* **2000**, *128*, 109–120. [CrossRef]
12. Attarchi, S.; Gloaguen, R. Improving the estimation of above ground biomass using dual polarimetric palsar and ETM+ data in the hyrcanian mountain forest (Iran). *Remote Sens.* **2014**, *6*, 3693–3715. [CrossRef]
13. Foody, G.M.; Boyd, D.S.; Cutler, M.E. Predictive relations of tropical forest biomass from landsat tm data and their transferability between regions. *Remote Sens. Environ.* **2003**, *85*, 463–474. [CrossRef]
14. Ghasemi, N.; Sahebi, M.R.; Mohammadzadeh, A. Biomass estimation of a temperate deciduous forest using wavelet analysis. *IEEE Trans. Geosci. Remote Sens.* **2013**, *51*, 765–776. [CrossRef]
15. Le Toan, T.; Beaudoin, A.; Riom, J.; Guyon, D. Relating forest biomass to sar data. *IEEE Trans. Geosci. Remote Sens.* **1992**, *30*, 403–411. [CrossRef]
16. Lu, D. The potential and challenge of remote sensing-based biomass estimation. *Int. J. Remote Sens.* **2006**, *27*, 1297–1328. [CrossRef]
17. Cartus, O.; Santoro, M.; Kellndorfer, J. Mapping forest aboveground biomass in the northeastern united states with alos palsar dual-polarization L-band. *Remote Sens. Environ.* **2012**, *124*, 466–478. [CrossRef]
18. Bharadwaj, P.S.; Kumar, S.; Kushwaha, S.; Bijker, W. Polarimetric scattering model for estimation of above ground biomass of multilayer vegetation using alos-palsar quad-pol data. *Phys. Chem. Earth Parts A/B/C* **2015**, *83*, 187–195. [CrossRef]
19. Saatchi, S.; Marlier, M.; Chazdon, R.L.; Clark, D.B.; Russell, A.E. Impact of spatial variability of tropical forest structure on radar estimation of aboveground biomass. *Remote Sens. Environ.* **2011**, *115*, 2836–2849. [CrossRef]
20. Lu, D.; Chen, Q.; Wang, G.; Liu, L.; Li, G.; Moran, E. A survey of remote sensing-based aboveground biomass estimation methods in forest ecosystems. *Int. J. Digit. Earth* **2016**, *9*, 63–105. [CrossRef]
21. Zhao, P.; Lu, D.; Wang, G.; Liu, L.; Li, D.; Zhu, J.; Yu, S. Forest aboveground biomass estimation in zhejiang province using the integration of landsat tm and alos palsar data. *Int. J. Appl. Earth Obs. Geoinf.* **2016**, *53*, 1–15. [CrossRef]
22. Atto, A.M.; Trouvé, E.; Nicolas, J.-M.; Lê, T.T. Wavelet operators and multiplicative observation models—Application to sar image time-series analysis. *IEEE Trans. Geosci. Remote Sens.* **2016**, *54*, 6606–6624. [CrossRef]
23. Cutler, M.E.J.; Boyd, D.S.; Foody, G.M.; Vetrivel, A. Estimating tropical forest biomass with a combination of sar image texture and landsat tm data: An assessment of predictions between regions. *ISPRS J. Photogramm. Remote Sens.* **2012**, *70*, 66–77. [CrossRef]
24. Hame, T.; Rauste, Y.; Antropov, O.; Ahola, H.A.; Kilpi, J. Improved mapping of tropical forests with optical and sar imagery, part II: Above ground biomass estimation. *IEEE J. Sel. Top. Appl. Earth Obs. Remote Sens.* **2013**, *6*, 92–101. [CrossRef]
25. Japan Aerospace Exploration Agency. *ALOS-2/Palsar-2 Level 1.1/1.5/2.1/3.1 Ceos SAR Product*; JAXA: Paris, France, 2014; p. 233.
26. Malenovský, Z.; Rott, H.; Cihlar, J.; Schaepman, M.E.; García-Santos, G.; Fernandes, R.; Berger, M. Sentinels for science: Potential of Sentinel-1, -2, and -3 missions for scientific observations of ocean, cryosphere, and land. *Remote Sens. Environ.* **2012**, *120*, 91–101. [CrossRef]
27. Sibanda, M.; Mutanga, O.; Rouget, M. Examining the potential of Sentinel-2 msi spectral resolution in quantifying above ground biomass across different fertilizer treatments. *ISPRS J. Photogramm. Remote Sens.* **2015**, *110*, 55–65. [CrossRef]
28. Korhonen, L.; Hadi; Packalen, P.; Rautiainen, M. Comparison of Sentinel-2 and landsat 8 in the estimation of boreal forest canopy cover and leaf area index. *Remote Sens. Environ.* **2017**, *195*, 259–274. [CrossRef]
29. Castillo, J.A.A.; Apan, A.A.; Maraseni, T.N.; Salmo, S.G., III. Estimation and mapping of above-ground biomass of mangrove forests and their replacement land uses in the philippines using sentinel imagery. *ISPRS J. Photogramm. Remote Sens.* **2017**, *134*, 70–85. [CrossRef]
30. Ali, I.; Cawkwell, F.; Dwyer, E.; Green, S. Modeling managed grassland biomass estimation by using multitemporal remote sensing data—A machine learning approach. *IEEE J. Sel. Top. Appl. Earth Obs. Remote Sens.* **2016**, *10*, 3254–3264. [CrossRef]

31. López-Serrano, P.M.; López-Sánchez, C.A.; Álvarez-González, J.G.; García-Gutiérrez, J. A comparison of machine learning techniques applied to landsat-5 tm spectral data for biomass estimation. *Can. J. Remote Sens.* **2016**, *42*, 690–705. [CrossRef]
32. Wu, C.; Shen, H.; Shen, A.; Deng, J.; Gan, M.; Zhu, J.; Xu, H.; Wang, K. Comparison of machine-learning methods for above-ground biomass estimation based on landsat imagery. *APPRES* **2016**, *10*. [CrossRef]
33. Hall, M.; Frank, E.; Holmes, G.; Pfahringer, B.; Reutemann, P.; Witten, I.H. The weka data mining software: An update. *SIGKDD Explor. Newsl.* **2009**, *11*, 10–18. [CrossRef]
34. Mohammadi, J.; Shataee, S. Possibility investigation of tree diversity mapping using landsat ETM+ data in the hyrcanian forests of iran. *Remote Sens. Environ.* **2010**, *114*, 1504–1512. [CrossRef]
35. Lee, J.-S.; Hoppel, K.W.; Mango, S.A.; Miller, A.R. Intensity and phase statistics of multilook polarimetric and interferometric sar imagery. *IEEE Trans. Geosci. Remote Sens.* **1994**, *32*, 1017–1028.
36. Tachikawa, T.; Kaku, M.; Iwasaki, A.; Gesch, D.B.; Oimoen, M.J.; Zhang, Z.; Danielson, J.J.; Krieger, T.; Curtis, B.; Haase, J. *ASTER Global Digital Elevation Model Version 2—Summary of Validation Results*; NASA: Washington, DC, USA, 2011.
37. Shimada, M.; Isoguchi, O.; Tadono, T.; Isono, K. Palsar radiometric and geometric calibration. *IEEE Trans. Geosci. Remote Sens.* **2009**, *47*, 3915–3932. [CrossRef]
38. Manna, S.; Nandy, S.; Chanda, A.; Akhand, A.; Hazra, S.; Dadhwal, V.K. Estimating aboveground biomass in avicennia marina plantation in indian sundarbans using high-resolution satellite data. *APPRES* **2014**, *8*. [CrossRef]
39. Patel, N.; Majumdar, A. Biomass estimation of shorea robusta with principal component analysis of satellite data. *J. For. Res.* **2010**, *21*, 469–474. [CrossRef]
40. Wicaksono, P.; Danoedoro, P.; Hartono; Nehren, U. Mangrove biomass carbon stock mapping of the karimunjawa islands using multispectral remote sensing. *Int. J. Remote Sens.* **2016**, *37*, 26–52. [CrossRef]
41. Jensen, J.R. *Introductory Digital Image Processing: A Remote Sensing Perspective*; Prentice-Hall, Inc.: Saddle River, NJ, USA, 1996.
42. Tucker, C.J. Red and photographic infrared linear combinations for monitoring vegetation. *Remote Sens. Environ.* **1979**, *8*, 127–150. [CrossRef]
43. Rouse, J.W., Jr.; Haas, R.; Schell, J.; Deering, D. Monitoring vegetation systems in the great plains with erts. In Proceedings of the Third Earth Resources Technology Satellite-1 Symposium, Washington, DC, USA, 10–14 December 1973; pp. 3010–3017.
44. Jiang, Z.; Huete, A.R.; Didan, K.; Miura, T. Development of a two-band enhanced vegetation index without a blue band. *Remote Sens. Environ.* **2008**, *112*, 3833–3845. [CrossRef]
45. Huete, A.R. A soil-adjusted vegetation index (savi). *Remote Sens. Environ.* **1988**, *25*, 295–309. [CrossRef]
46. Bannari, A.; Huete, A.R.; Morin, D.; Zagolski, F. Effets de la couleur et de la brillance du sol sur les indices de végétation. *Int. J. Remote Sens.* **1996**, *17*, 1885–1906. [CrossRef]
47. Breiman, L. Random forests. *Mach. Learn.* **2001**, *45*, 5–32. [CrossRef]
48. Cutler, D.R.; Edwards, T.C.; Beard, K.H.; Cutler, A.; Hess, K.T.; Gibson, J.; Lawler, J.J. Random forests for classification in ecology. *Ecology* **2007**, *88*, 2783–2792. [CrossRef] [PubMed]
49. Pelletier, C.; Valero, S.; Inglada, J.; Champion, N.; Dedieu, G. Assessing the robustness of random forests to map land cover with high resolution satellite image time series over large areas. *Remote Sens. Environ.* **2016**, *187*, 156–168. [CrossRef]
50. Friedman, J.; Hastie, T.; Tibshirani, R. *The Elements of Statistical Learning*; Springer: New York, NY, USA, 2001.
51. Gislason, P.O.; Benediktsson, J.A.; Sveinsson, J.R. Random forests for land cover classification. *Pattern Recognit. Lett.* **2006**, *27*, 294–300. [CrossRef]
52. Rodriguez-Galiano, V.F.; Ghimire, B.; Rogan, J.; Chica-Olmo, M.; Rigol-Sanchez, J.P. An assessment of the effectiveness of a random forest classifier for land-cover classification. *ISPRS J. Photogramm. Remote Sens.* **2012**, *67*, 93–104. [CrossRef]
53. Stevens, F.R.; Gaughan, A.E.; Linard, C.; Tatem, A.J. Disaggregating census data for population mapping using random forests with remotely-sensed and ancillary data. *PLoS ONE* **2015**, *10*. [CrossRef] [PubMed]
54. Tien Bui, D.; Bui, Q.-T.; Nguyen, Q.-P.; Pradhan, B.; Nampak, H.; Trinh, P.T. A hybrid artificial intelligence approach using gis-based neural-fuzzy inference system and particle swarm optimization for forest fire susceptibility modeling at a tropical area. *Agric. For. Meteorol.* **2017**, *233*, 32–44. [CrossRef]

55. Drucker, H.; Burges, C.J.; Kaufman, L.; Smola, A.J.; Vapnik, V. Support vector regression machines. In Proceedings of the Neural Information Processing Systems 1996, Denver, CO, USA, 2–7 December 1996; pp. 155–161.
56. Smola, A.J.; Schölkopf, B. A tutorial on support vector regression. *Stat. Comput.* **2004**, *14*, 199–222. [CrossRef]
57. Tien Bui, D.; Pradhan, B.; Lofman, O.; Revhaug, I. Landslide susceptibility assessment in vietnam using support vector machines, decision tree, and naïve bayes models. *Math. Probl. Eng.* **2012**, *2012*. [CrossRef]
58. Tien Bui, D.; Tuan, T.A.; Klempe, H.; Pradhan, B.; Revhaug, I. Spatial prediction models for shallow landslide hazards: A comparative assessment of the efficacy of support vector machines, artificial neural networks, kernel logistic regression, and logistic model tree. *Landslides* **2016**, *13*, 361–378. [CrossRef]
59. Pham, B.T.; Tien Bui, D.; Dholakia, M.B.; Prakash, I.; Pham, H.V. A comparative study of least square support vector machines and multiclass alternating decision trees for spatial prediction of rainfall-induced landslides in a tropical cyclones area. *Geotech. Geol. Eng.* **2016**, *34*, 1807–1824. [CrossRef]
60. Hoang, N.-D.; Tien Bui, D. A novel relevance vector machine classifier with cuckoo search optimization for spatial prediction of landslides. *J. Comput. Civ. Eng.* **2016**, *30*, 04016001. [CrossRef]
61. Hoang, N.-D.; Bui, D.T.; Liao, K.-W. Groutability estimation of grouting processes with cement grouts using differential flower pollination optimized support vector machine. *Appl. Soft Comput.* **2016**, *45*, 173–186. [CrossRef]
62. Petropoulos, G.P.; Kalaitzidis, C.; Prasad Vadrevu, K. Support vector machines and object-based classification for obtaining land-use/cover cartography from hyperion hyperspectral imagery. *Comput. Geosci.* **2011**, *41*, 99–107. [CrossRef]
63. Wu, C.; Tao, H.; Zhai, M.; Lin, Y.; Wang, K.; Deng, J.; Shen, A.; Gan, M.; Li, J.; Yang, H. Using nonparametric modeling approaches and remote sensing imagery to estimate ecological welfare forest biomass. *J. For. Res.* **2018**, *29*, 151–161. [CrossRef]
64. Mountrakis, G.; Im, J.; Ogole, C. Support vector machines in remote sensing: A review. *ISPRS J. Photogramm. Remote Sens.* **2011**, *66*, 247–259. [CrossRef]
65. Vapnik, V. *The Nature of Statistical Learning Theory*; Springer Science & Business Media: Berlin, Germany, 2013.
66. Tien Bui, D.; Anh Tuan, T.; Hoang, N.-D.; Quoc Thanh, N.; Nguyen, B.D.; Van Liem, N.; Pradhan, B. Spatial prediction of rainfall-induced landslides for the lao cai area (Vietnam) using a novel hybrid intelligent approach of least squares support vector machines inference model and artificial bee colony optimization. *Landslides* **2017**, *14*, 447–458. [CrossRef]
67. Tien Bui, D.; Le, K.-T.T.; Nguyen, V.C.; Le, H.D.; Revhaug, I. Tropical forest fire susceptibility mapping at the cat ba national park area, hai phong city, vietnam, using gis-based kernel logistic regression. *Remote Sens.* **2016**, *8*, 347. [CrossRef]
68. Hu, X.; Weng, Q. Estimating impervious surfaces from medium spatial resolution imagery using the self-organizing map and multi-layer perceptron neural networks. *Remote Sens. Environ.* **2009**, *113*, 2089–2102. [CrossRef]
69. Tien Bui, D.; Pradhan, B.; Lofman, O.; Revhaug, I.; Dick, O.B. Landslide susceptibility assessment in the hoa binh province of vietnam: A comparison of the levenberg-marquardt and bayesian regularized neural networks. *Geomorphology* **2012**, *171*, 12–29. [CrossRef]
70. Civco, D.L. Artificial neural networks for land-cover classification and mapping. *Int. J. Geogr. Inf. Syst.* **1993**, *7*, 173–186. [CrossRef]
71. Mas, J.F. Mapping land use/cover in a tropical coastal area using satellite sensor data, gis and artificial neural networks. *Estuar. Coast. Shelf Sci.* **2004**, *59*, 219–230. [CrossRef]
72. Pham, T.D.; Yoshino, K.; Bui, D.T. Biomass estimation of sonneratia caseolaris (l.) engler at a coastal area of hai phong city (Vietnam) using alos-2 palsar imagery and gis-based multi-layer perceptron neural networks. *GISci. Remote Sens.* **2017**, *54*, 329–353. [CrossRef]
73. Haykin, S. *Neural Networks: A Comprehensive Foundation*, 2nd ed.; Prentice Hall: Upper Saddle River, NJ, USA, 1998.
74. Tien Bui, D.; Pradhan, B.; Nampak, H.; Bui, Q.-T.; Tran, Q.-A.; Nguyen, Q.-P. Hybrid artificial intelligence approach based on neural fuzzy inference model and metaheuristic optimization for flood susceptibilitgy modeling in a high-frequency tropical cyclone area using gis. *J. Hydrol.* **2016**, *540*, 317–330. [CrossRef]

75. Were, K.; Bui, D.T.; Dick, Ø.B.; Singh, B.R. A comparative assessment of support vector regression, artificial neural networks, and random forests for predicting and mapping soil organic carbon stocks across an afromontane landscape. *Ecol. Indic.* **2015**, *52*, 394–403. [CrossRef]
76. Verrelst, J.; Muñoz, J.; Alonso, L.; Delegido, J.; Rivera, J.P.; Camps-Valls, G.; Moreno, J. Machine learning regression algorithms for biophysical parameter retrieval: Opportunities for Sentinel-2 and -3. *Remote Sens. Environ.* **2012**, *118*, 127–139. [CrossRef]
77. Verrelst, J.; Rivera, J.P.; Moreno, J.; Camps-Valls, G. Gaussian processes uncertainty estimates in experimental Sentinel-2 lai and leaf chlorophyll content retrieval. *ISPRS J. Photogramm. Remote Sens.* **2013**, *86*, 157–167. [CrossRef]
78. Fassnacht, F.; Hartig, F.; Latifi, H.; Berger, C.; Hernández, J.; Corvalán, P.; Koch, B. Importance of sample size, data type and prediction method for remote sensing-based estimations of aboveground forest biomass. *Remote Sens. Environ.* **2014**, *154*, 102–114. [CrossRef]
79. Verrelst, J.; van der Tol, C.; Magnani, F.; Sabater, N.; Rivera, J.P.; Mohammed, G.; Moreno, J. Evaluating the predictive power of sun-induced chlorophyll fluorescence to estimate net photosynthesis of vegetation canopies: A scope modeling study. *Remote Sens. Environ.* **2016**, *176*, 139–151. [CrossRef]
80. Campos-Taberner, M.; García-Haro, F.J.; Camps-Valls, G.; Grau-Muedra, G.; Nutini, F.; Crema, A.; Boschetti, M. Multitemporal and multiresolution leaf area index retrieval for operational local rice crop monitoring. *Remote Sens. Environ.* **2016**, *187*, 102–118. [CrossRef]
81. Rasmussen, C.E.; Williams, C.K. *Gaussian Processes for Machine Learning*; MIT Press Cambridge: Cambridge, MA, USA, 2006.
82. Viana, H.; Aranha, J.; Lopes, D.; Cohen, W.B. Estimation of crown biomass of pinus pinaster stands and shrubland above-ground biomass using forest inventory data, remotely sensed imagery and spatial prediction models. *Ecol. Model.* **2012**, *226*, 22–35. [CrossRef]
83. Byrd, K.B.; O'Connell, J.L.; Di Tommaso, S.; Kelly, M. Evaluation of sensor types and environmental controls on mapping biomass of coastal marsh emergent vegetation. *Remote Sens. Environ.* **2014**, *149*, 166–180. [CrossRef]
84. Chai, T.; Draxler, R.R. Root mean square error (rmse) or mean absolute error (mae)?—Arguments against avoiding rmse in the literature. *Geosci. Model. Dev.* **2014**, *7*, 1247–1250. [CrossRef]
85. Pham, T.D.; Yoshino, K. Aboveground biomass estimation of mangrove species using alos-2 palsar imagery in hai phong city, vietnam. *APPRES* **2017**, *11*. [CrossRef]
86. Kohavi, R.; John, G.H. Wrappers for feature subset selection. *Artif. Intell.* **1997**, *97*, 273–324. [CrossRef]
87. Fiol, G.D.; Haug, P.J. Classification models for the prediction of clinicians' information needs. *J. Biomed. Inf.* **2009**, *42*, 82–89. [CrossRef] [PubMed]
88. Shen, M.; Tang, Y.; Klein, J.; Zhang, P.; Gu, S.; Shimono, A.; Chen, J. Estimation of aboveground biomass using in situ hyperspectral measurements in five major grassland ecosystems on the tibetan plateau. *J. Plant Ecol.* **2008**, *1*, 247–257. [CrossRef]
89. Pargal, S.; Fararoda, R.; Rajashekar, G.; Balachandran, N.; Réjou-Méchain, M.; Barbier, N.; Jha, C.; Pélissier, R.; Dadhwal, V.; Couteron, P. Inverting aboveground biomass? Canopy texture relationships in a landscape of forest mosaic in the western ghats of india using very high resolution cartosat imagery. *Remote Sens.* **2017**, *9*, 228. [CrossRef]
90. Zheng, D.; Rademacher, J.; Chen, J.; Crow, T.; Bresee, M.; Le Moine, J.; Ryu, S.-R. Estimating aboveground biomass using landsat 7 ETM+ data across a managed landscape in northern wisconsin, USA. *Remote Sens. Environ.* **2004**, *93*, 402–411. [CrossRef]
91. Lu, D.; Mausel, P.; Brondízio, E.; Moran, E. Relationships between forest stand parameters and landsat tm spectral responses in the brazilian amazon basin. *For. Ecol. Manag.* **2004**, *198*, 149–167. [CrossRef]
92. Li, S.; Wu, H.; Wan, D.; Zhu, J. An effective feature selection method for hyperspectral image classification based on genetic algorithm and support vector machine. *Knowl. Based Syst.* **2011**, *24*, 40–48. [CrossRef]
93. Deka, P.C. Support vector machine applications in the field of hydrology: A review. *Appl. Soft Comput.* **2014**, *19*, 372–386.
94. Jakubowski, M.K.; Guo, Q.; Kelly, M. Tradeoffs between lidar pulse density and forest measurement accuracy. *Remote Sens. Environ.* **2013**, *130*, 245–253. [CrossRef]
95. Kim, Y.H.; Im, J.; Ha, H.K.; Choi, J.-K.; Ha, S. Machine learning approaches to coastal water quality monitoring using goci satellite data. *GISci. Remote Sens.* **2014**, *51*, 158–174. [CrossRef]

96. Siegmann, B.; Jarmer, T. Comparison of different regression models and validation techniques for the assessment of wheat leaf area index from hyperspectral data. *Int. J. Remote Sens.* **2015**, *36*, 4519–4534. [CrossRef]
97. Axelsson, C.; Skidmore, A.K.; Schlerf, M.; Fauzi, A.; Verhoef, W. Hyperspectral analysis of mangrove foliar chemistry using plsr and support vector regression. *Int. J. Remote Sens.* **2013**, *34*, 1724–1743. [CrossRef]
98. Goh, J.; Miettinen, J.; Chia, A.S.; Chew, P.T.; Liew, S.C. Biomass estimation in humid tropical forest using a combination of alos palsar and spot 5 satellite imagery. *Asian J. Geoinform.* **2014**, *13*.
99. Aslan, A.; Rahman, A.F.; Warren, M.W.; Robeson, S.M. Mapping spatial distribution and biomass of coastal wetland vegetation in indonesian papua by combining active and passive remotely sensed data. *Remote Sens. Environ.* **2016**, *183*, 65–81. [CrossRef]
100. Ranson, K.J.; Guoqing, S. Mapping biomass of a northern forest using multifrequency sar data. *IEEE Trans. Geosci. Remote Sens.* **1994**, *32*, 388–396. [CrossRef]
101. Basuki, T.M.; Skidmore, A.K.; Hussin, Y.A.; Van Duren, I. Estimating tropical forest biomass more accurately by integrating alos palsar and landsat-7 ETM+ data. *Int. J. Remote Sens.* **2013**, *34*, 4871–4888. [CrossRef]
102. Luo, S.; Wang, C.; Xi, X.; Pan, F.; Peng, D.; Zou, J.; Nie, S.; Qin, H. Fusion of airborne lidar data and hyperspectral imagery for aboveground and belowground forest biomass estimation. *Ecol. Indic.* **2017**, *73*, 378–387. [CrossRef]
103. Chave, J.; Andalo, C.; Brown, S.; Cairns, M.A.; Chambers, J.Q.; Eamus, D.; Fölster, H.; Fromard, F.; Higuchi, N.; Kira, T.; et al. Tree allometry and improved estimation of carbon stocks and balance in tropical forests. *Oecologia* **2005**, *145*, 87–99. [CrossRef] [PubMed]